# $CO_2$ hydrogenation at atmospheric pressure and low temperature using plasma-enhanced catalysis over supported cobalt oxide catalysts

*Maria Ronda-Lloret[‡], Yaolin Wang[‡†], Paula Oulego[††], Gadi Rothenberg, Xin Tu[†]* and N. Raveendran Shiju**

* Corresponding authors: xin.tu@liverpool.ac.uk; n.r.shiju@uva.nl

Van 't Hoff Institute for Molecular Sciences, University of Amsterdam, Science Park 904, 1090GD Amsterdam (The Netherlands)

† Department of Electrical Engineering and Electronics, University of Liverpool, Liverpool L69 3GJ, United Kingdom

†† Department of Chemical and Environmental Engineering, University of Oviedo, C/ Julián Clavería, s/n. E-33071, Oviedo, Spain

Keywords: Green chemistry, plasma catalysis, methanol synthesis, cobalt oxide, $CO_2$ conversion

‡ M. Ronda-Lloret and Y. Wang contributed equally for this paper.

**Abstract.** $CO_2$ is a promising renewable, cheap and abundant C1 feedstock for producing valuable chemicals, such as CO and methanol. In conventional reactors, due to thermodynamic constraints, converting $CO_2$ to methanol requires high temperature and pressure, typically 250 °C and 20 bar. Non-thermal plasma is a better option, as it can convert $CO_2$ at near-ambient temperature and pressure. Adding a catalyst to such plasma setups can enhance conversion and selectivity. However, we know little about the effects of catalysts in such systems. Here, we study $CO_2$ hydrogenation in a dielectric barrier discharge (DBD) plasma-catalysis setup at ambient conditions using MgO, $\gamma$-$Al_2O_3$ and a series of $Co_xO_y$/MgO catalysts. While all three catalyst types enhanced $CO_2$ conversion, $Co_xO_y$/MgO gave the best results, converting up to 35% of the $CO_2$ and reaching the highest methanol yield (10%). Control experiments showed that the basic MgO support is more active than the acidic $\gamma$-$Al_2O_3$, and that MgO-supported cobalt oxide catalysts improve the selectivity towards methanol. The methanol yield can be modified by changing the metal loading. Overall, our study shows the utility of plasma-catalysis for $CO_2$ conversion under mild conditions, reducing the energy footprint of $CO_2$ recycling processes.

## Introduction

The increasing amount of $CO_2$ in the atmosphere is a global problem.[1–3] Yet $CO_2$ is also an important chemical resource that should not be thrown away. Ideally, we should use it as a raw material to make valuable products. This can be done via carbon capture, either from the atmosphere or from industrial flue-gases, followed by a chemical reaction. [4–6] Typically this would involve a catalytic process.

Hydrogenation is a versatile option for $CO_2$ valorization, provided that renewable hydrogen is used.[7–11] One can alter the reaction parameters ($CO_2/H_2$ ratio, temperature and pressure), and the catalyst composition to control the product distribution.[12] $CO_2$ can be hydrogenated to carbon

monoxide (CO), methane ($CH_4$), methanol ($CH_3OH$), ethanol ($C_2H_5OH$) and lower olefins ($C_2^{=}$–$C_4^{=}$). Of these, methanol is especially interesting, as it is a precursor for formaldehyde, dimethyl ether, gasoline and olefins.[13,14] Methanol is also an efficient energy carrier.[15–17] $CO_2$ hydrogenation to methanol (Equation 1) is exothermic, and therefore favored at low temperatures. This reaction is also favored at high pressures because fewer molecules are produced. However, the high thermodynamic stability of $CO_2$ ($\Delta G^0$ = –394.4 kJ mol$^{-1}$) requires high temperatures for high conversion. At < 200 °C, the endothermic reverse-water gas shift (RWGS, Equation 2) reaction is favored. The side product, CO, is itself a useful building block for making a variety of chemicals.[12,18] Therefore, $CO_2$ hydrogenation to methanol is typically performed at 250 °C and 20 bar.[14,19]

$$CO_2 + 3\,H_2 \longleftrightarrow CH_3OH + H_2O \quad \Delta H_{25\,°C} = -\,49.5 \text{ kJ mol}^{-1} \quad (1)$$

$$CO_2 + H_2 \longleftrightarrow CO + H_2O \quad \Delta H_{25\,°C} = 41.2 \text{ kJ mol}^{-1} \quad (2)$$

Yet there is an alternative to thermal-catalysis: Plasma-enhanced catalysis can be used for converting $CO_2$ to useful chemicals at near-ambient temperatures and pressures.[20–29] In non-thermal plasmas, high-energy electrons (with an electron temperature of 1–10 eV) activate stable molecules by collisions, while the bulk gas temperature remains low.[30,31] Catalysts can be introduced into these systems to increase the conversion and control the selectivity.[19,32] Among the different types of plasma discharges, the dielectric barrier discharge (DBD) is the most common option in plasma-catalysis. This is because DBD reactors usually run at low temperatures and atmospheric pressure, reducing operating costs and complexity.[30,33,34]

Despite the growing research activity in plasma-enhanced catalysis, we still don't understand the relationship between the catalyst properties and overall reaction performance.[35–38] This is due to the variety of the reactions and plasma configurations, which lead to different plasma species and

different plasma-catalyst interactions.[39-42] Here, we study the effect of basic catalysts (MgO and $Co_xO_y$/MgO catalysts) on conversion and product selectivity during $CO_2$ hydrogenation. We ran the reaction in a water cooled DBD plasma-catalysis setup, at 35 °C and ambient pressure. Further, we tested γ-$Al_2O_3$ to check if the enhanced adsorption of acidic $CO_2$ on basic supports is also valid under plasma conditions.[43] We observed that $CO_2$ conversion can be increased by using basic materials, and that the production of methanol is related to the metal loading and the dispersion of metal-support interface sites in $Co_xO_y$/MgO catalysts.

## Experimental section

**Materials and instrumentation.** Powder X-Ray diffraction (XRD) analyses were carried out on a MiniFlex II diffractometer using Cu Kα radiation(X-ray tube set at 30 kV and 15 mA). The XRD patterns were recorded between 2θ = 20–80°, with a turning speed of 2.5 °·$min^{-1}$. $N_2$ adsorption-desorption analyses were performed on a Thermo Scientific Surfer instrument at 77 K. The samples were pre-treated under vacuum at 200 °C for 6 h. Surface areas were calculated using the Brunauer–Emmett–Teller (BET) method, and the mesoporosity was analyzed using the Barrett, Joyner and Halenda (BJH) method. Hydrogen temperature programmed reduction ($H_2$-TPR) profiles were obtained using a TPDRO Series 1100 from Thermo Scientific, following the procedure previously reported by Ronda-Lloret *et al.*[6] High-resolution transmission electron microscopy (HRTEM) micrographs and transmission electron microscopy coupled with Energy-dispersive X-ray spectroscopy (STEM-EDS) were measured on a JEOL-JEM 2100F microscope running at a voltage of 200 kV. X-ray photoelectron spectroscopy (XPS) analyses were performed with a SPECS Phoibos 100 MCD5 hemispherical electron analyzer operating in a constant pass energy. The analysis details were described previously in Matthaiou *et al.*[44]

**Procedure for catalyst synthesis.** Samples containing different percentages of cobalt metal loadings (5, 10, 15 and 20 wt.%) were prepared by wet impregnation using $Co(NO_3)_2 \cdot 6H_2O$ (99%, Acros Organics) as metal oxide precursor and MgO (Sigma-Aldrich) as support.[6] After impregnation, the materials were dried at 120 °C for 2 h and then calcined in a muffle furnace at 450 °C for 4 h . Bulk $Co_3O_4$ was prepared by dissolving 2.7 g of $Na_2CO_3$ and 0.05 g of polyethylene glycol in 25 mL of water, followed by the rapid addition of 2.42 g of $Co(NO_3)_2 \cdot 6H_2O$ dissolved in 25 mL of water.[45] The mixture was stirred for 3 h at room temperature. Afterwards, the precipitate was collected by centrifugation, and washed several times with water and ethanol. After drying at 65 °C for 6 h in a vacuum oven, the sample was calcined in air at 300 °C for 3 h.

**Plasma setup and plasma-catalytic tests.** The plasma-catalytic tests were performed in a coaxial DBD reactor with a 50 mm discharge length and a 1 mm discharge gap (Scheme 1). Circulating water was used as the ground electrode and cooling system (Grant LT Ecocool 150) to keep the reaction temperature at 35 °C. An AC high voltage power supply (with a peak-to-peak voltage of up to 30 kV) was used to ignite the plasma with a fixed frequency of 9.2 kHz. $CO_2$ and $H_2$ ($H_2/CO_2$ = 3:1) were used as reactants with a total flow rate of 28 $mL \cdot min^{-1}$. The catalysts (500 mg) were fully packed in the discharge area, and the products were analyzed after the plasma reaction for 1.5 h.

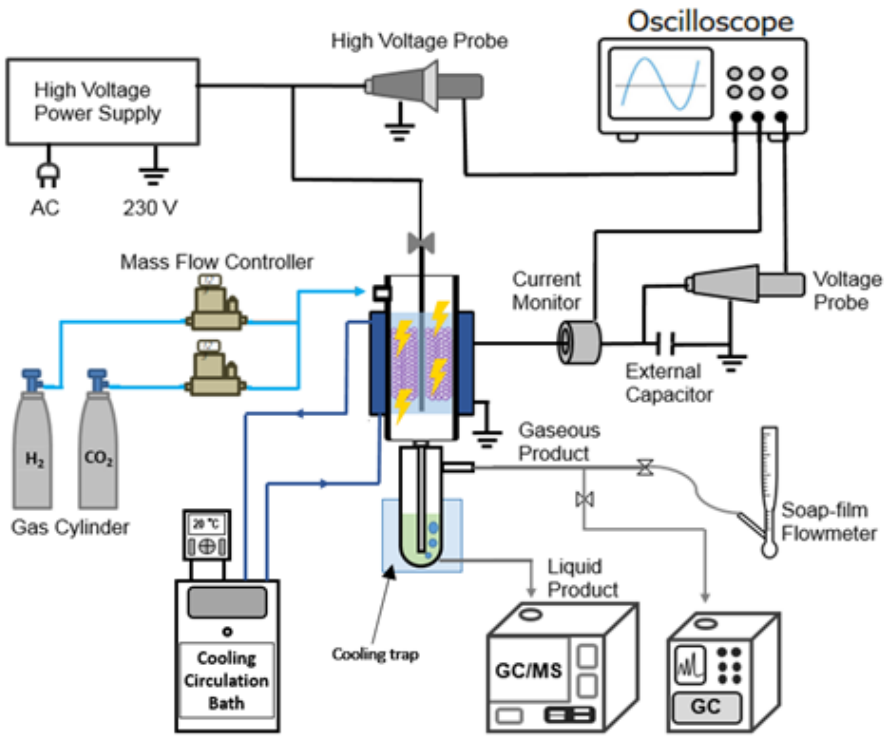


**Scheme 1.** Diagram of the plasma-catalysis DBD reactor, showing the analysis, feed, and cooling units.

The applied voltage and current of the DBD were measured by a high-voltage probe (TESTEC, HVP-15HF), and a current monitor (Bergoz, CT-E0.5), respectively. A four-channel digital oscilloscope (Tektronix, MDO 3024) was used to collect all the electrical signals, and the plotted Q-U Lissajous figures could monitor the discharge powers in real time using a homemade system. A fiber optical thermometer (Omega, FOB102) was used to monitor the temperature of the discharge area. The reaction products were analyzed using an Agilent 7820A gas chromatography system equipped with a flame ionization detector (FID) and a thermal conductivity detector (TCD). A Molecular Sieve 5A (60-80 mesh) column (HP MOLESIEVE) was used for the separation of $H_2$ and CO, while an HP-PLOT/Q column was used for $CO_2$, $CH_4$ and $C_2$-$C_4$ hydrocarbons. The measurement error was less than 4%, determined by triplicate measurements.

**Parameter definition.**

The conversions of $CO_2$ ($X_{CO_2}$) and $H_2$ ($X_{H_2}$) are defined as

$$X_{CO_2}\ (\%) = \frac{\text{moles of } CO_2 \text{ converted}}{\text{moles of initial } CO_2} \times 100 \quad (3)$$

$$X_{H_2}\ (\%) = \frac{\text{moles of } H_2 \text{ converted}}{\text{moles of initial } H_2} \times 100 \quad (4)$$

The selectivity of gaseous products (CO, $CH_4$ and $C_mH_n$) is calculated according to Eqs 5, 6 and 7:

$$S_{CO}\ (\%) = \frac{\text{moles of CO produced}}{\text{moles of } CO_2 \text{ converted}} \times 100 \quad (5)$$

$$S_{CH_4}\ (\%) = \frac{\text{moles of } CH_4 \text{ produced}}{\text{moles of } CO_2 \text{ converted}} \times 100 \quad (6)$$

$$S_{C_mH_n}\ (\%) = \frac{\text{moles of } C_mH_n \text{ produced}}{\text{moles of } CO_2 \text{ converted}} \times 100 \quad (7)$$

The selectivity of the liquid products is calculated as

$$S_{liquid\ products}\ (\%) = 100 - (S_{CO}+S_{CH_4}+S_{C_mH_n}) \quad (8)$$

The selectivity of $C_xH_yO_z$ is defined as:

$$S_{CxHyOz}\ (\%) = \text{mol \% of carbon atoms in } C_xH_yO_z \times \text{Eq. 8} \quad (9)$$

The energy efficiency is defined as:

$$\text{Energy efficiency (mmol·kW}^{-1}\text{·h}^{-1}) = \frac{\text{converted product (mmol·h}^{-1})}{\text{discharge power (kW)}} \quad (10)$$

**Results and discussion**

**Catalyst synthesis.** We tested MgO and γ-$Al_2O_3$ as packing materials in the DBD plasma. The same materials were also used as supports for the cobalt oxide catalysts with different cobalt metal

loadings. These catalysts were prepared by wet impregnation, followed by drying and calcination. We also prepared bulk $Co_3O_4$ by mixing polyethylene glycol and cobalt nitrate hexahydrate in water (the detailed procedures are described in the experimental section).

**Catalyst characterisation.** The XRD patterns of the fresh $Co_xO_y$/MgO samples show the characteristic diffraction peaks of MgO at 2θ = 36.9°, 42.9°, 62.2°, 74.6° and 78.6° (Figure S1a).[46] The characteristic peaks of $Co_3O_4$ and CoO are not visible, as they overlap with those of MgO.[47,48] HRTEM) and STEM-EDS images of 15% $Co_xO_y$/MgO show that cobalt oxide particles are highly dispersed over the support (Figures 1 and 2). The average size of cobalt oxide nanoparticles was 27.7 ± 11.5 nm. Moreover, HRTEM shows clear lattice fringes with an interplanar distance of 0.24 and 0.28–0.29 nm (Figure 1b–1c), assigned to the (311) and (220) planes of cobalt oxide nanoparticles, respectively.[49] The selected-area electron diffraction (SAED) pattern shows diffraction rings characteristic of a polycrystalline material, corresponding to MgO ((220), (200) and (311)) and cobalt oxide nanoparticles (311) planes.[49,50]

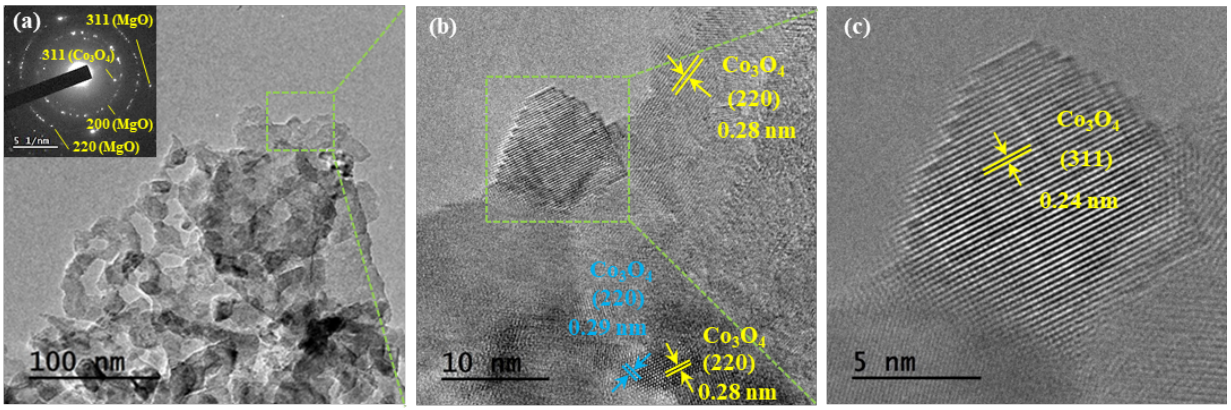


**Figure 1.** Representative TEM images of 15% $Co_xO_y$/MgO. (a) TEM micrograph and its corresponding SAED pattern (inset), showing a set of diffraction rings characteristic of MgO and $Co_3O_4$ planes. (b) and (c) magnified HRTEM images of 15% $Co_xO_y$/MgO. The yellow and blue lines mark the lattice fringes of the planes of cobalt oxide nanoparticles.

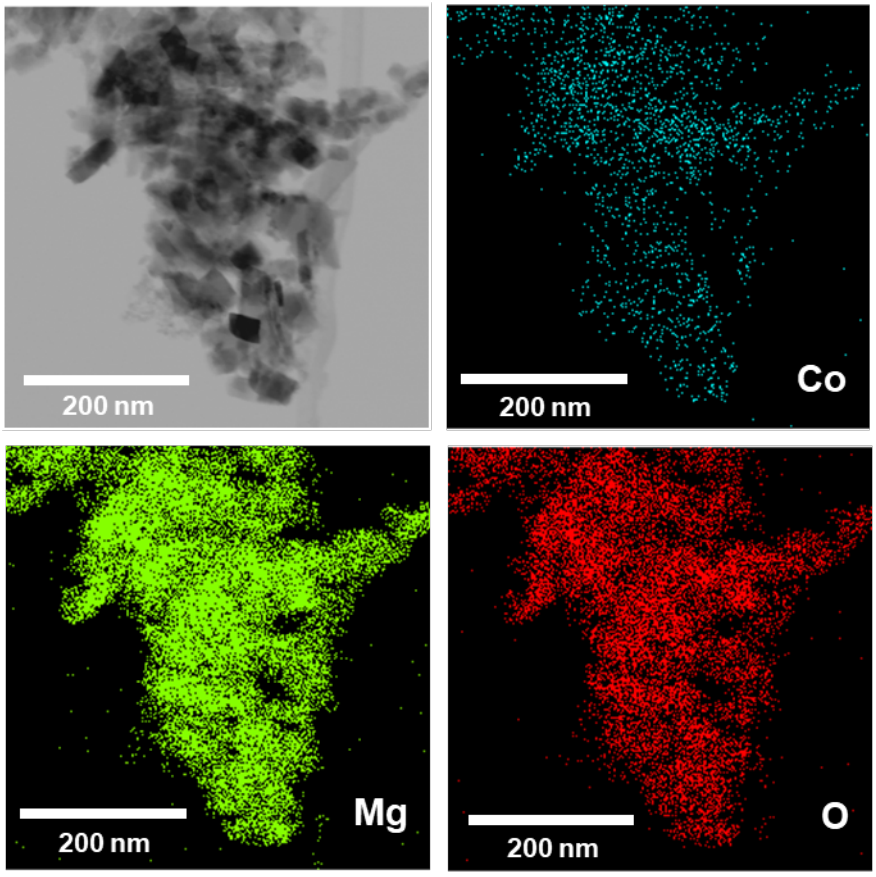


**Figure 2.** STEM-EDS analysis of fresh 15% $Co_xO_y$/MgO catalyst. Representative STEM image (top left) and the corresponding EDS elemental mappings of cobalt (top right), magnesium (bottom left) and oxygen (bottom right), showing the dispersion of the cobalt particles on the support.

We then studied the surface composition of the catalysts with X-ray photoelectron spectroscopy (XPS). The Co 2p spectra of the $Co_xO_y$/MgO catalysts are characterized by the doublet of two spin-orbit components, Co $2p_{3/2}$ and Co $2p_{1/2}$ (Figure 3).[51,52] The relative atomic percentage for $Co_3O_4$ species is higher than for CoO species for all fresh catalysts, indicating the predominance of $Co_3O_4$ on the

surface (Table S1). This reveals that $Co_3O_4$-CoO/MgO interface sites are available on the catalyst surface as active centers for $CO_2$ hydrogenation. The O 1s, C 1s and Mg 2s spectra of 15% $Co_xO_y$/MgO catalyst, as well as details on the binding energies are included in the supporting information (Figure S2 and Tables S2–S5).

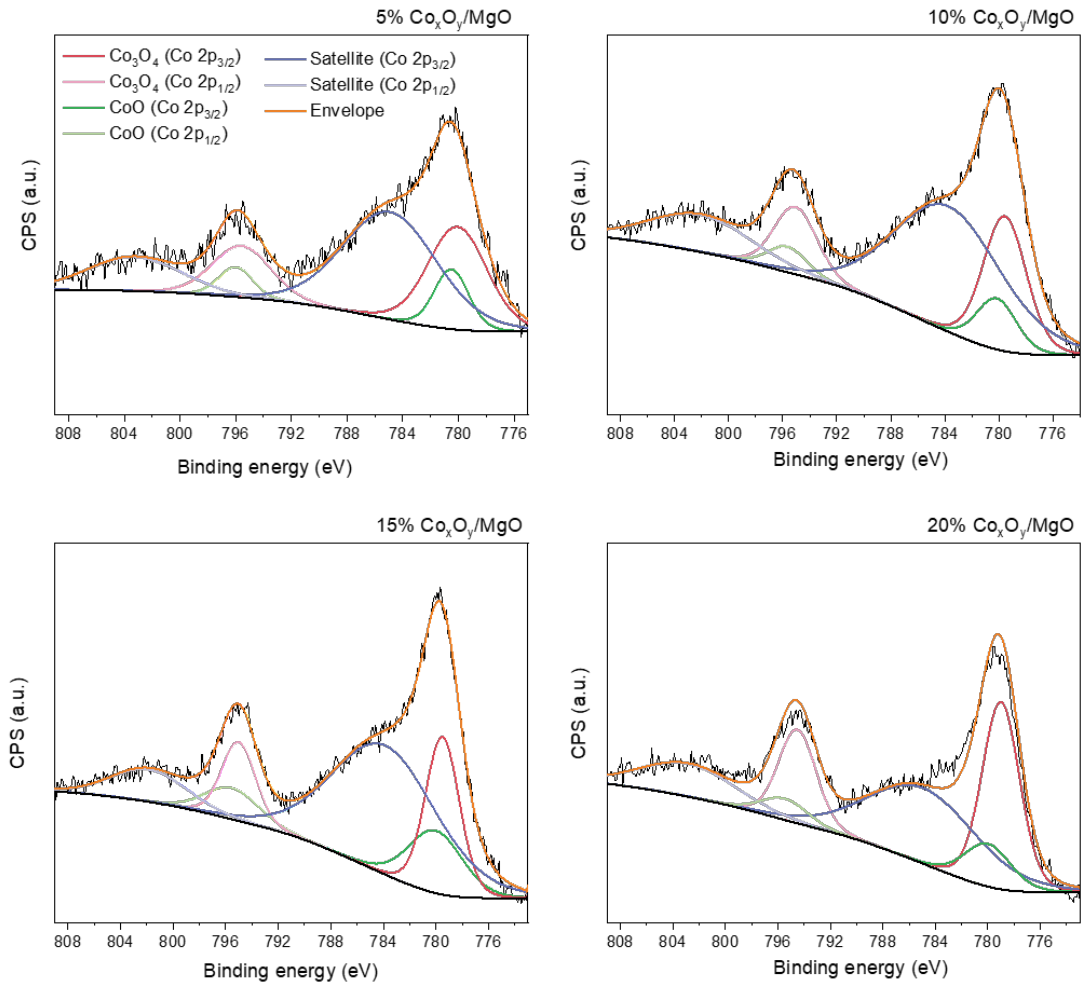


**Figure 3.** Co 2p XPS spectra of the fresh $Co_xO_y$/MgO catalysts.

The $H_2$-TPR profiles of the as-prepared catalysts (Figure S3, bottom profiles) show two regions. The low temperature region (150–450 °C) is assigned to the reduction of 'free' $Co_3O_4$ (supported cobalt oxide that is interacting weakly with the support, thus not forming a stable compound). This reduction peak contains two or more contributions, corresponding to the $Co_3O_4$ step wise reduction

sequence where $Co_3O_4$ is reduced to CoO, and CoO is reduced to metallic cobalt at higher temperatures. The reduction of $Co_3O_4$ species with different interaction with the support can also lead to different contributions in the reduction peak.[53] They are less defined in the 20% $Co_xO_y$/MgO sample, most likely because the first contribution shifts to a higher temperature. This reflects the presence of larger cobalt oxide particles, which are harder to reduce than smaller ones.[54]

In the high temperature region (500–1000 °C), the 5% $Co_xO_y$/MgO reduction profile clearly shows a small reduction peak at 500–600 °C, ascribed to the reduction of $MgCo_2O_4$ species.[53] Above 700 °C, all the samples show the reduction of stable (Co,Mg)O solid solution species.[55] These peaks overlap at higher metal loadings. In some cases the (Co,Mg)O solid solution is only partially reduced.

The nitrogen adsorption-desorption isotherms of the fresh catalysts (Figure S4) are similar to type IV, with a hysteresis feature characteristic of mesoporous materials.[56] The BET surface area and pore volume values increase with the metal loading up to 15% (Table 1). 20% $Co_xO_y$/MgO catalyst doesn´t follow this trend, indicating the presence of larger cobalt oxide particles that block the pores and decrease the surface area. HRTEM analysis of this sample confirmed the presence of larger cobalt oxide particles compared to the 15% sample (Figure S5a).

**Table 1.** BET surface area, cumulative pore volume and average pore diameter (from BJH analysis) values derived from nitrogen sorption isotherms.

| Catalyst | $S_{BET}$ ($m^2 \cdot g^{-1}$) | Pore volume ($cm^3 \cdot g^{-1}$) | Average pore diameter (nm) |
|---|---|---|---|
| 5% $Co_xO_y$/MgO | 33 | 0.2 | 56 |
| 10% $Co_xO_y$/MgO | 37 | 0.4 | 44 |

| | | | |
|---|---|---|---|
| 15% $Co_xO_y$/MgO | 39 | 0.6 | 49 |
| 20% $Co_xO_y$/MgO | 26 | 0.3 | 26 |

**Catalytic tests.** We performed the $CO_2$ hydrogenation reaction in a coaxial DBD reactor, maintained at 35 °C using circulating cooling water. The plasma operated at atmospheric pressure and 10 W. Previous plasma-catalytic $CO_2$ hydrogenation studies show that excess of hydrogen in the reaction mixture, up to 4:1 $H_2/CO_2$ molar ratio, typically increases the conversion.[22,25,57] In addition, two recent studies reported higher methanol yields at 3:1 $H_2/CO_2$ molar ratio.[26,27] To favor $CO_2$ conversion and methanol formation, we set the $H_2/CO_2$ molar ratio to 3:1.

First, we tested plasma alone (Figure S6), which gave 15% $CO_2$ conversion and 7% $H_2$ conversion (the plasma background reaction). The products were mainly CO (71% selectivity) and methanol (22%), as well as 2% of methane and 6% of acetic acid (all results are averages of triplicate measurements).

We then tested the effect of different packing materials. MgO and $\gamma$-$Al_2O_3$ are conventional supports, which are usually inactive in thermal-catalysis. However, these materials enhanced the activity when introduced in the DBD plasma chamber even at the mild reaction conditions mentioned above (Figure S6). MgO showed significantly higher conversion values (27% $CO_2$ conversion and 13% $H_2$ conversion) than plasma alone. CO selectivity also increased, from 71% with plasma only to 84% with MgO. Alumina also gave higher $CO_2$ and $H_2$ conversion (17% and 7%, respectively) than plasma alone, and higher CO selectivity (80%).

The changes in conversion and product distribution when placing a packing material in the plasma discharge can be explained by examining the possible reaction pathways. Typically, in a $CO_2/H_2$ mixture in DBD plasma (without catalyst), the predominant reaction for the consumption

of $CO_2$ is the effective electron impact dissociation to CO (R1).[58,59] The electron impact vibrational excitation of $CO_2$ makes a minor contribution, due to its tendency to react back to ground $CO_2$. Similarly, $H_2$ is consumed by electron impact dissociation to two hydrogen radicals (R2). CO and H• radicals can start several reactions that lead to formaldehyde $CH_2O$ (R3-R9). $CH_2O$ is then hydrogenated to methanol (R10 and R11),[26,58] while water is also produced (R12 and R13).[58]

$$CO_2 + e^- \longrightarrow CO + O + e^- \quad \text{(R1)}$$
$$H_2 + e^- \longrightarrow H + H + e^- \quad \text{(R2)}$$
$$CO + H \longrightarrow CHO \quad \text{(R3)}$$
$$CHO + CHO \longrightarrow CH_2O + CO \quad \text{(R4)}$$
$$CO + e^- \longrightarrow C + O + e^- \quad \text{(R5)}$$
$$C + H \longrightarrow CH + e^- \quad \text{(R6)}$$
$$CH + H \longrightarrow CH_2 \quad \text{(R7)}$$
$$CH_2 + O \longrightarrow CH_2O \quad \text{(R8)}$$
$$CO_2 + CH_2 \longrightarrow CH_2O + CO \quad \text{(R9)}$$
$$CH_2O + H \longrightarrow CH_2OH \quad \text{(R10)}$$
$$CH_2OH + H \longrightarrow CH_3OH \quad \text{(R11)}$$
$$O + H \longrightarrow OH + e^- \quad \text{(R12)}$$
$$OH + H_2 \longrightarrow H_2O + H \quad \text{(R13)}$$

When combining plasma and a catalyst, previous work found that both gas-phase reactions and plasma-assisted surface reactions contribute to the conversion and selectivity.[60] Gas-phase reactions involve reactions R1 to R11. In addition, the CO derived from $CO_2$ dissociation in gas-phase can adsorb on the catalyst surface and react with adsorbed hydrogen to form to methanol, as represented in Figure 4a.[60–62] $CO_2$ can also adsorb on the catalyst surface, as confirmed elsewhere with the detection of carbonates using *in-situ* spectroscopy analysis.[23,60,61] Both ground and excited $CO_2$ can be adsorbed, although the contribution of excited $CO_2$ can be neglected because it is prone to be quenched or relaxed by the surface.[26,63]

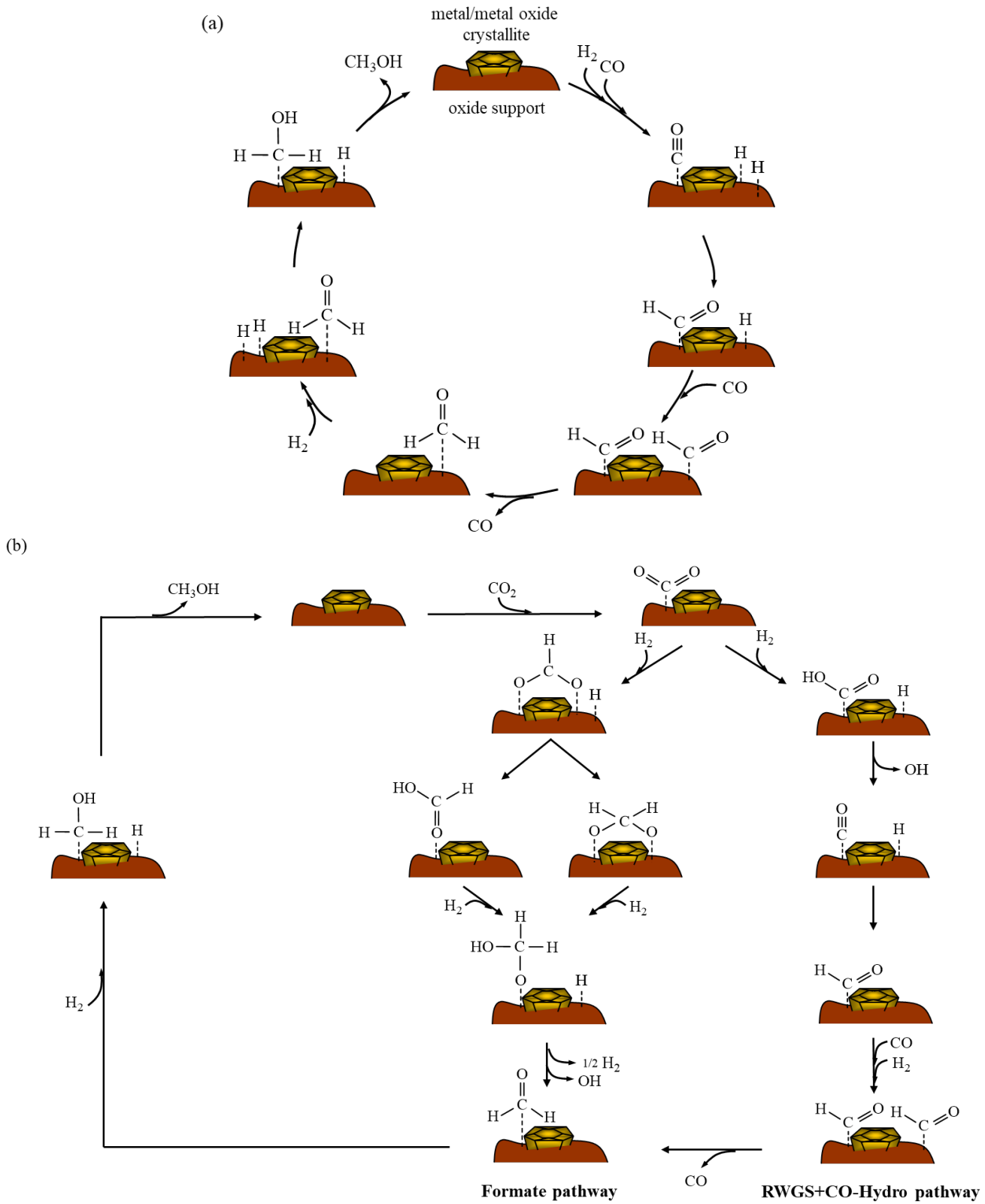


**Figure 4.** Proposed reaction pathways for methanol production on a catalyst surface in $H_2/CO_2$ DBD plasma, where a) CO or b) $CO_2$ are adsorbed on the catalyst surface.[60–65]

Adsorbed $CO_2$ is then hydrogenated to either hydrocarboxyl (HOCO) or formate ($HCOO^-$) species (Figure 4b).[64] The decomposition of HOCO to CO initiates the so-called RWGS+CO-Hydro pathway.[64,65] The formate pathway can also take place, where $HCOO^-$ is hydrogenated in several steps. Both pathways lead to the formation of $H_2CO$, which is hydrogenated to methanol via the methoxy ($H_3CO$) intermediate.[62,66,67]

The increase in $CO_2$ conversion and CO selectivity when placing MgO or $Al_2O_3$ in the plasma chamber is ascribed to their ability to adsorb $CO_2$ and perform both plasma-assisted surface reactions and gas-phase reactions. MgO shows higher conversion than $Al_2O_3$, which is related to their acid-base properties. $CO_2$ is attracted better by the basic sites of solid surfaces because of its acidic property.[43] MgO is significantly more basic than $Al_2O_3$ and therefore it has a higher $CO_2$ adsorption capacity.[68,69] Both materials increase CO selectivity, indicating that they promote the RWGS pathway. These metal oxides do not have strong affinity to CO and $H_2$/H species, hindering the formation of methanol.[64]

Shifting the selectivity towards methanol requires a stronger binding energy of CO and hydrogen, as well as the participation of a considerable amount of adsorbed hydrogen in the reaction pathway. Cobalt-based catalysts are active in $CO_2$ hydrogenation to ethanol, methane and larger hydrocarbons.[70–73] Therefore, we tested the influence of MgO-supported cobalt oxide catalysts with different metal loadings on the reaction performance (Figure 5). Our results show an improved conversion when using $Co_xO_y$/MgO catalysts, which is partially ascribed to their ability to promote surface reactions. These catalysts also gave a narrower product distribution. We also observed acetic acid (<1%), ethanol (trace), and methane (<2%).

The 5% $Co_xO_y$/MgO catalyst converted 30% of $CO_2$ and 13% of $H_2$, giving 92% selectivity to CO and 6% of methanol. Compared to MgO, it only improved $CO_2$ conversion, therefore increasing

CO selectivity. The low amount of cobalt oxide in this catalyst does not shift the product distribution to methanol.

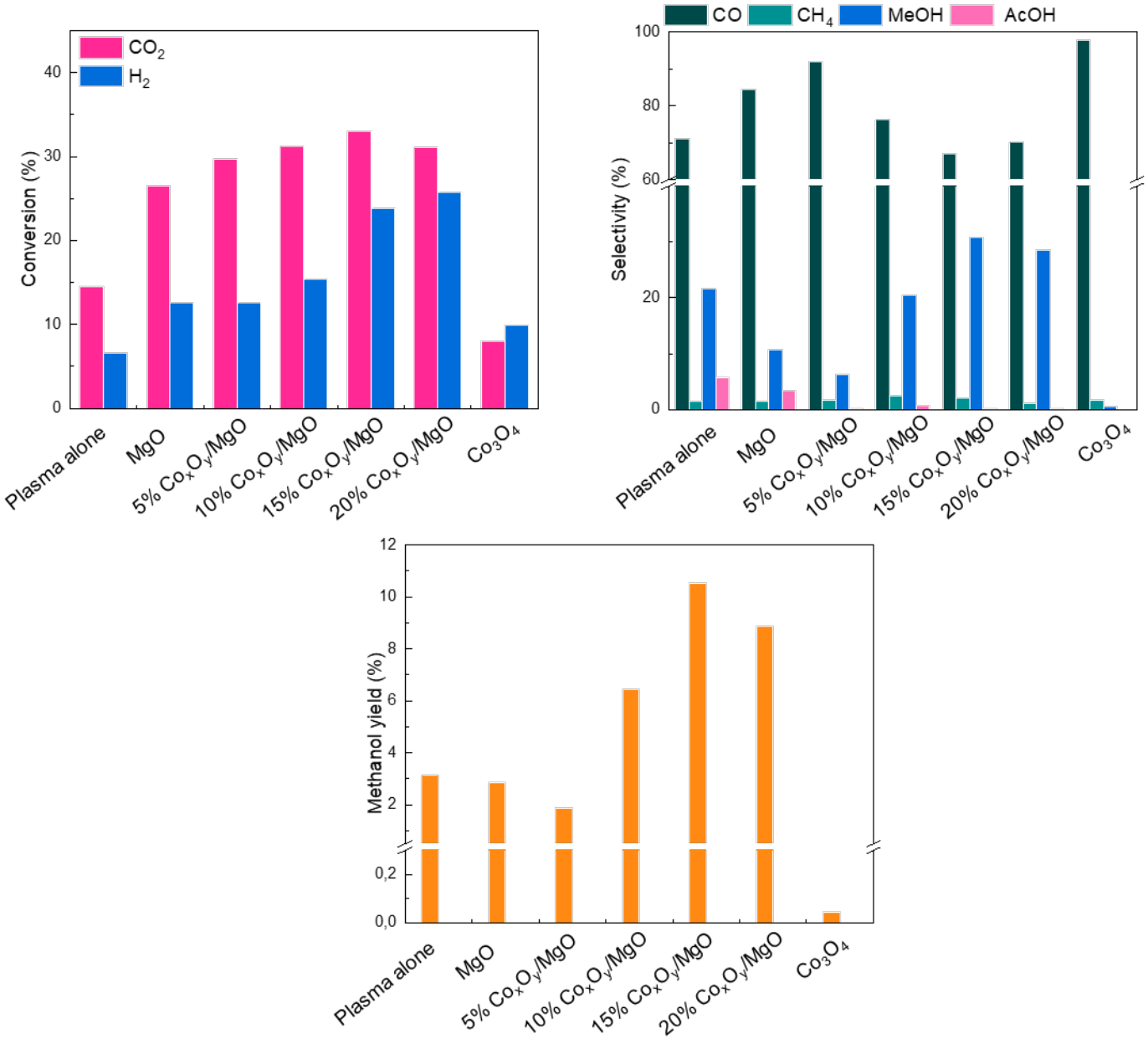


**Figure 5.** $CO_2$ and $H_2$ conversion, selectivity and methanol yield plots of plasma alone, MgO, $Co_xO_y$/MgO with different cobalt metal loadings and unsupported $Co_3O_4$. Reaction conditions: 35 °C, atmospheric pressure, 500 mg catalyst, total flow 28 mL·min$^{-1}$, $H_2/CO_2$ molar ratio 3:1, discharge power 10 W, reaction time 1.5 h.

The 10% $Co_xO_y$/MgO catalyst showed 31% $CO_2$ conversion and 15% $H_2$ conversion, as well as 76% selectivity to CO and 20% selectivity to methanol. Further increasing the cobalt loading to 15% improved the conversion values to 33% $CO_2$ and 24% $H_2$, and the methanol selectivity to 31%. This catalyst gave the highest methanol yield (>10%). This indicates that catalysts with high metal loading increase the amount of adsorbed CO and hydrogen available for reaction, facilitating methanol production. Increasing the metal loading to 20% gave 31% $CO_2$ conversion and 9% methanol yield.

From these results, we conclude that the quantity and dispersion of the $Co_3O_4$/CoO sites play an important role in the activity enhancement and methanol selectivity, in agreement with previous studies.[64,72] $CO_2$ conversion and methanol selectivity increase when increasing the metal loading from 5% to 15%. The BET surface area and pore volume also increase when increasing the metal loading up to 15% (see Table 1). This indicates that a good dispersion of the metal oxide nanoparticles on the support favors $CO_2$ conversion. Higher metal loadings (20%) lead to larger cobalt oxide particles (as confirmed by HRTEM), which block the pores of the support and decrease the catalyst surface area. This reduces the metal oxide dispersion compared to lower metal loadings, inhibiting further increase on conversion and methanol production.

For comparison, we tested unsupported $Co_3O_4$ (Figure 5). This gave lower conversion (8% $CO_2$ and 10% $H_2$) than the supported $Co_xO_y$/MgO catalysts, with CO as the main product (98% selectivity). The decrease in methanol formation when using $Co_3O_4$ emphasizes the importance of metal oxide-support interface sites for methanol synthesis.

Compared to plasma only, the combination of plasma and any tested catalyst improves the energy efficiency of CO production (Figure S7), reaching its maximum when using 10%

$Co_xO_y$/MgO catalyst (509 mmol CO·kW$^{-1}$·h$^{-1}$). The energy efficiency of methanol production is improved when a considerable metal loading of cobalt is used (10, 15 and 20% $Co_xO_y$/MgO catalysts). The optimal methanol energy efficiency was obtained with 15% $Co_xO_y$/MgO (190.8 mmol MeOH·kW$^{-1}$·h$^{-1}$), which is related to the balance between a considerable amount of $Co_3O_4$/CoO sites and their good dispersion on the support. None of these catalysts were active in thermal activity tests, showing the importance of the plasma-catalytic hybrid approach in activating $CO_2$ at near-ambient temperatures. In addition, we studied the stability of the 15% $Co_xO_y$/MgO catalyst under reaction conditions (Figure S8). The catalyst performance was stable up to 4.5 h, with only a slight deactivation at the start of the reaction.

**Plasma and catalyst interactions.** We studied the effect of the plasma discharge on the physicochemical properties of the $Co_xO_y$/MgO catalysts. The XRD patterns of the spent catalysts correspond to those of the fresh catalysts (Figure S1b). HRTEM and STEM images of 15% $Co_xO_y$/MgO spent catalyst (Figures S8 and S9) discard the sintering of cobalt oxide particles, since the average size of cobalt oxide nanoparticles (24.5 ± 7.6 nm) is very similar to the fresh catalyst (27.7 ± 11.5 nm). HRTEM images of spent 20% $Co_xO_y$/MgO (Figure S5b) do not show a significant change on the particle size neither. In general, the surface area and porosity of the spent catalysts are similar to the fresh ones (Table S7). The 20% sample shows the largest increase in BET surface area (from 26 to 35 $m^2 \cdot g^{-1}$), and the 15% sample shows the largest increase on pore volume and average pore size. In addition, XPS analysis of all catalysts shows that the $I_{Co}/I_{Mg}$ ratio remains unaltered (Table S6), indicating that the dispersion of cobalt oxide on the support is not affected by the plasma.

XPS and $H_2$-TPR analysis of the spent catalysts indicate the partial reduction of $Co_3O_4$ surface species under $CO_2/H_2$ plasma. For the samples with a cobalt metal loading lower than 20%, the XPS Co 2p peaks corresponding to CoO species increase in intensity, while the ones of $Co_3O_4$ decrease (Figure 6 and Table S1). The 20% $Co_xO_y$/MgO catalyst doesn't show major reduction after plasma exposure, as the $Co_3O_4$ and CoO peak intensities remain similar to the fresh catalyst. In the reduction profiles (Figure S3), the first contribution in the low temperature region becomes less intense for the spent 5, 10 and 15% $Co_xO_y$/MgO catalysts. This contribution corresponds to the easily reducible $Co_3O_4$ species. There are no major changes in the reduction profile of 20% $Co_xO_y$/MgO, indicating that this sample contains larger $Co_3O_4$ particles that are harder to reduce.

We conclude that the catalysts with a cobalt metal loading lower than 20% are significantly reduced from $Co_3O_4$ to CoO in the hydrogen-rich plasma environment. Nevertheless, we cannot exclude the formation of metallic cobalt due to plasma exposure. Since all spent catalysts were stored in air prior to characterization, we cannot detect metallic cobalt in XPS and $H_2$-TPR analysis.

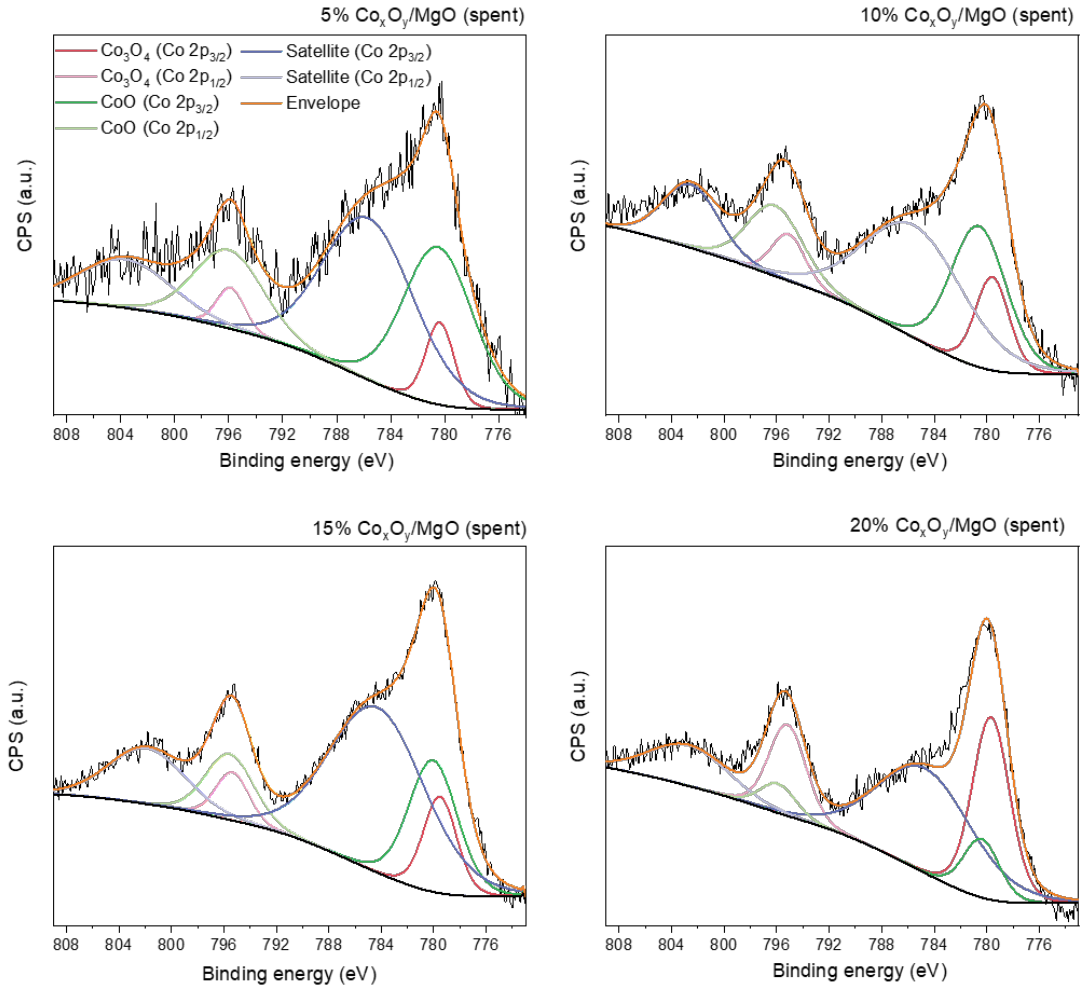


**Figure 6.** Co 2p XPS spectra of the spent $Co_xO_y$/MgO catalysts.

We also studied the effect of the catalysts in the plasma discharge properties, which in turn might affect the reaction performance. Figure S10a shows the current signals of the discharge with and without packing material. The intensity and density of the current pulses of the discharge follow the order of 15% $Co_xO_y$/MgO > plasma alone > MgO > $Co_3O_4$, which agrees with the order of $CO_2$ conversion. Packing MgO or $Co_3O_4$ into the discharge gap weakens the formation of micro-discharges compared to plasma alone. The 15% $Co_xO_y$/MgO catalyst enhances the discharge, as evidenced by the increase in the current pulse, therefore favoring the formation of radicals and

vibrationally excited species that can participate in the reaction.[74–76] In addition, the Q-V Lissajous plot (Figure S10b) in the presence of a packing material is very similar to the one of plasma alone, remaining with an elliptical shape. We find that the change on the cobalt loading of the $Co_xO_y$/MgO catalysts does not affect the discharge, as the electrical signals are almost the same. Thus, we attribute the difference in product selectivity when using packing materials to their properties and to the promotion of surface reactions on the metal-support interface sites (see Figure 5 above).

**Conclusion**

In this study, we show the potential of plasma-enhanced catalysis for $CO_2$ hydrogenation reactions at ambient conditions. Packing a catalyst in a DBD plasma discharge enhances the conversion and narrows the product distribution of $CO_2$ hydrogenation. We found that the basicity of MgO support enhances the conversion of $CO_2$ compared to more acidic supports. These supports promote the production of CO as main product. When testing $Co_xO_y$/MgO catalysts, the quantity and dispersion of metal-support interface sites play an important role in the activity enhancement and methanol selectivity. Although CO is the main product, the catalysts with higher cobalt metal loadings and a good cobalt oxide dispersion favor methanol production. The most active catalyst was 15 wt.% $Co_xO_y$/MgO, which converted 33% of $CO_2$ and 24% of $H_2$ near room temperature and at atmospheric pressure. This catalyst gave 10% of methanol yield, the highest among the tested materials. Further increase of the metal loading leads to larger cobalt oxide particles that block the pores, giving lower $CO_2$ conversion and less methanol. Finding correlations between catalyst properties and reaction performance remains a challenge in this field. We hope that this study will help in the rational design of materials for plasma-enhanced catalysis applications.

ASSOCIATED CONTENT

**Supporting Information**.

The following files are available free of charge.

XRD patterns of the fresh and spent catalysts; XPS data of the fresh and spent catalysts; temperature programmed reduction profiles of the fresh and spent catalysts; nitrogen adsorption-desorption isotherms of the fresh catalysts; HRTEM and STEM-EDS images of the spent 15% $Co_xO_y$/MgO catalyst; HRTEM images of the fresh and spent 20% $Co_xO_y$/MgO catalyst; plasma-catalytic tests of plasma alone, MgO and γ-$Al_2O_3$; energy efficiency values of all catalysts; stability test of 15% $Co_xO_y$/MgO catalyst; plasma electrical diagnostics (current signals, Q-V Lissajous plots and calculated discharge properties) of plasma alone, MgO, 15% $Co_xO_y$/MgO and $Co_3O_4$ (PDF).

AUTHOR INFORMATION

Corresponding Authors

N. Raveendran Shiju, Van 't Hoff Institute for Molecular Sciences, University of Amsterdam, Science Park 904, 1090GD Amsterdam, The Netherlands

E-mail: n.r.shiju@uva.nl

ORCID: 0000-0001-7943-5864

Xin Tu, Department of Electrical Engineering and Electronics, University of Liverpool, Liverpool L69 3GJ, United Kingdom

E-mail: xin.tu@liverpool.ac.uk

ORCID：0000-0002-6376-0897

Author Contributions

The manuscript was written through contributions of all authors. All authors have given approval to the final version of the manuscript.

ACKNOWLEDGMENT

M. Ronda-Lloret, G. Rothenberg and N.R. Shiju thank the Netherlands Organization for Scientific Research (NWO) for the grant "Developing novel catalytic materials for converting $CO_2$, methane and ethane to high-value chemicals in a hybrid plasma-catalytic reactor" (China.15.119). X. Tu acknowledges the funding from the European Union (EU) and Horizon 2020 research and innovation programme under the Marie Sklodowska-Curie Action (Grant Number 823745). Y. Wang acknowledges the European Union (EU) and Horizon 2020 funding awarded under the Marie Sklodowska-Curie Action to the EUROPAH Consortium (Grant Number 722346). P. Oulego thanks the Spanish Ministry of Science, Innovation and Universities (MICIU) (Project MCIU-19-RTI2018-094218-B-I00) and European Union (FEDER) for funding. P. Oulego acknowledges the technical support provided by Scientific and Technical Services of the University of Oviedo.

REFERENCES

(1) Vallero, D. A. Air Pollution Biogeochemistry. In *Air Pollution Calculations*; Elsevier Inc., 2019; pp 175–206. https://doi.org/10.1016/b978-0-12-814934-8.00008-9.

(2) Nejat, P.; Jomehzadeh, F.; Taheri, M. M.; Gohari, M.; Muhd, M. Z. A Global Review of Energy Consumption, $CO_2$ Emissions and Policy in the Residential Sector (with an Overview of the Top Ten $CO_2$ Emitting Countries). *Renew. Sustain. Energy Rev.* **2015**, *43*, 843–862. https://doi.org/10.1016/j.rser.2014.11.066.

(3) Hartmann, D. L. Anthropogenic Climate Change. In *Global Physical Climatology (Second Ed.)*; Elsevier Inc., 2016; pp 397–425. https://doi.org/10.1016/B978-0-12-328531-7.00013-X.

(4) Sanz-Pérez, E. S.; Murdock, C. R.; Didas, S. A.; Jones, C. W. Direct Capture of $CO_2$ from Ambient Air. *Chem. Rev.* **2016**, *116* (19), 11840–11876. https://doi.org/10.1021/acs.chemrev.6b00173.

(5) Kothandaraman, A.; Nord, L.; Bolland, O.; Herzog, H. J.; McRae, G. J. Comparison of Solvents for Post-Combustion Capture of $CO_2$ by Chemical Absorption. *Energy Procedia* **2009**, *1*, 1373–1380. https://doi.org/10.1016/j.egypro.2009.01.180.

(6) Ronda- Lloret, M.; Marakatti, V. S.; Sloof, W. G.; Delgado, J. J.; Sepúlveda- Escribano, A.; Ramos- Fernandez, E. V.; Rothenberg, G.; Shiju, N. R. Butane Dry Reforming Catalyzed by Cobalt Oxide Supported on $Ti_2AlC$ MAX Phase. *ChemSusChem* **2020**, *13*. https://doi.org/10.1002/cssc.202001633.

(7) Gibson, T. L.; Kelly, N. A. Optimization of Solar Powered Hydrogen Production Using Photovoltaic Electrolysis Devices. *Int. J. Hydrogen Energy* **2008**, *33* (21), 5931–5940. https://doi.org/10.1016/j.ijhydene.2008.05.106.

(8) Selamet, Ö. F.; Becerikli, F.; Mat, M. D.; Kaplan, Y. Development and Testing of a Highly Efficient Proton Exchange Membrane (PEM) Electrolyzer Stack. *Int. J. Hydrogen Energy* **2011**, *36* (17), 11480–11487. https://doi.org/10.1016/j.ijhydene.2011.01.129.

(9) Wood, A.; He, H.; Joia, T.; Krivy, M.; Steedman, D. Communication—Electrolysis at High Efficiency with Remarkable Hydrogen Production Rates. *J. Electrochem. Soc.* **2016**, *163* (5), F327–F329. https://doi.org/10.1149/2.0341605jes.

(10) Gnanakumar, E. S.; Chandran, N.; Kozhevnikov, I. V.; Grau-Atienza, A.; Ramos Fernández, E. V.; Sepulveda-Escribano, A.; Shiju, N. R. Highly Efficient Nickel-Niobia Composite Catalysts for Hydrogenation of $CO_2$ to Methane. *Chem. Eng. Sci.* **2019**, *194*, 2–9. https://doi.org/10.1016/j.ces.2018.08.038.

(11) Ramos-Fernandez, E. V.; Shiju, N. R.; Rothenberg, G. Understanding the Solar-Driven Reduction of CO2 on Doped Ceria. *RSC Adv.* **2014**, *4* (32), 16456. https://doi.org/10.1039/c4ra01242a.

(12) Ronda- Lloret, M.; Rothenberg, G.; Shiju, N. R. A Critical Look at Direct Catalytic Hydrogenation of Carbon Dioxide to Olefins. *ChemSusChem* **2019**, *12* (17), 3896–3914. https://doi.org/10.1002/cssc.201900915.

(13) Olsbye, U.; Svelle, S.; Bjrgen, M.; Beato, P.; Janssens, T. V. W.; Joensen, F.; Bordiga, S.; Lillerud, K. P. Conversion of Methanol to Hydrocarbons: How Zeolite Cavity and Pore Size Controls Product Selectivity. *Angew. Chem. Int. Ed.* **2012**, *51* (24), 5810–5831. https://doi.org/10.1002/anie.201103657.

(14) Bowker, M. Methanol Synthesis from $CO_2$ Hydrogenation. *ChemCatChem* **2019**, *11* (17), 4238–4246. https://doi.org/10.1002/cctc.201900401.

(15) Choudhury, J. New Strategies for $CO_2$-to-Methanol Conversion. *ChemCatChem* **2012**, *4* (5), 609–611. https://doi.org/10.1002/cctc.201100495.

(16) Olah, G. A. Beyond Oil and Gas: The Methanol Economy. *Angew. Chem. Int. Ed.* **2005**, *44* (18), 2636–2639. https://doi.org/10.1002/anie.200462121.

(17) Liu, X.; Wang, M.; Zhou, C.; Zhou, W.; Cheng, K.; Kang, J.; Zhang, Q.; Deng, W.; Wang, Y. Selective Transformation of Carbon Dioxide into Lower Olefins with a Bifunctional Catalyst Composed of $ZnGa_2O_4$ and SAPO-34. *Chem. Commun.* **2017**, *54* (2), 140–143. https://doi.org/10.1039/c7cc08642c.

(18) Torres Galvis, H. M.; de Jong, K. P. Catalysts for Production of Lower Olefins from Synthesis Gas: A Review. *ACS Catal.* **2013**, *3* (9), 2130–2149. https://doi.org/10.1021/cs4003436.

(19) Liu, M.; Yi, Y.; Wang, L.; Guo, H.; Bogaerts, A. Hydrogenation of Carbon Dioxide to Value-Added Chemicals by Heterogeneous Catalysis and Plasma Catalysis. *Catalysts* **2019**, *9*, 275. https://doi.org/10.3390/catal9030275.

(20) Xu, S.; Chansai, S.; Stere, C.; Inceesungvorn, B.; Goguet, A.; Wangkawong, K.; Taylor, S. F. R.; Al-Janabi, N.; Hardacre, C.; Martin, P. A.; Fan, X. Sustaining Metal–Organic Frameworks for Water–Gas Shift Catalysis by Non-Thermal Plasma. *Nat. Catal.* **2019**, *2* (2), 142–148. https://doi.org/10.1038/s41929-018-0206-2.

(21) Zeng, Y.; Tu, X. Plasma-Catalytic Hydrogenation of $CO_2$ for the Cogeneration of CO and $CH_4$ in a Dielectric Barrier Discharge Reactor: Effect of Argon Addition. *J. Phys. D. Appl. Phys.* **2017**, *50* (18), 184004. https://doi.org/10.1088/1361-6463/aa64bb.

(22) Liu, L.; Das, S.; Chen, T.; Dewangan, N.; Ashok, J.; Xi, S.; Borgna, A.; Li, Z.; Kawi, S. Low Temperature Catalytic Reverse Water-Gas Shift Reaction over Perovskite Catalysts in DBD Plasma. *Appl. Catal. B Environ.* **2020**, *265* (118573). https://doi.org/10.1016/j.apcatb.2019.118573.

(23) Sun, Y.; Li, J.; Chen, P.; Wang, B.; Wu, J.; Fu, M.; Chen, L.; Ye, D. Reverse Water-Gas Shift in a Packed Bed DBD Reactor: Investigation of Metal-Support Interface towards a Better Understanding of Plasma Catalysis. *Appl. Catal. A Gen.* **2020**, *591*, 117407. https://doi.org/10.1016/j.apcata.2019.117407.

(24) Li, J.; Sun, Y.; Wang, B.; Xiao, H.; Wu, J.; Chen, L.; Fu, M.; Ye, D. Effect of Plasma on Catalytic Conversion of $CO_2$ with Hydrogen over Pd/ZnO in a Dielectric Barrier Discharge Reactor. *J. Phys. D. Appl. Phys.* **2019**, *52*, 244001. https://doi.org/10.1088/1361-6463/ab111b.

(25) Eliasson, B.; Kogelschatz, U.; Xue, B.; Zhou, L. M. Hydrogenation of Carbon Dioxide to Methanol with a Discharge-Activated Catalyst. *Ind. Eng. Chem. Res.* **1998**, *37* (8), 3350–3357. https://doi.org/10.1021/ie9709401.

(26) Wang, L.; Yi, Y.; Guo, H.; Tu, X. Atmospheric Pressure and Room Temperature Synthesis of Methanol through Plasma-Catalytic Hydrogenation of $CO_2$. *ACS Catal.* **2018**, *8* (1), 90–100. https://doi.org/10.1021/acscatal.7b02733.

(27) Men, Y. L.; Liu, Y.; Wang, Q.; Luo, Z. H.; Shao, S.; Li, Y. B.; Pan, Y. X. Highly Dispersed Pt-Based Catalysts for Selective $CO_2$ Hydrogenation to Methanol at Atmospheric Pressure. *Chem. Eng. Sci.* **2019**, *200*, 167–175. https://doi.org/10.1016/j.ces.2019.02.004.

(28) George, A.; Shen, B.; Craven, M.; Wang, Y.; Kang, D.; Wu, C.; Tu, X. A Review of Non-Thermal Plasma Technology : A Novel Solution for $CO_2$ Conversion and Utilization. *Renew. Sustain. Energy Rev.* **2021**, *135*, 109702. https://doi.org/10.1016/j.rser.2020.109702.

(29) Bogaerts, A.; Tu, X.; Whitehead, J. C.; Centi, G.; Lefferts, L.; Guaitella, O.; Azzolina-jury, F.; Kim, H.; Murphy, A. B.; Schneider, W. F.; Nozaki, T.; Jason, C. The 2020 Plasma Catalysis Roadmap. *J. Phys. D. Appl. Phys.* **2020**, *53*, 443001. https://doi.org/doi.org/10.1088/1361-6463/ab9048.

(30) Snoeckx, R.; Bogaerts, A. Plasma Technology – a Novel Solution for $CO_2$ Conversion? *Chem. Soc. Rev.* **2017**, *46* (19), 5805–5863. https://doi.org/10.1039/c6cs00066e.

(31) Mehta, P.; Barboun, P.; Go, D. B.; Hicks, J. C.; Schneider, W. F. Catalysis Enabled by Plasma Activation of Strong Chemical Bonds: A Review. *ACS Energy Lett.* **2019**, *4* (5), 1115–1133. https://doi.org/10.1021/acsenergylett.9b00263.

(32) Devid, E.; Ronda-Lloret, M.; Huang, Q.; Rothenberg, G.; Raveendran Shiju, N.; Kleyn, A. Conversion of $CO_2$ by Non- Thermal Inductively-Coupled Plasma Catalysis. *Chinese J. Chem. Phys.* **2020**, *33*, 243. https://doi.org/10.1063/1674-0068/cjcp2004040.

(33) Tao, X.; Bai, M.; Li, X.; Long, H.; Shang, S.; Yin, Y.; Dai, X. $CH_4$-$CO_2$ Reforming by Plasma - Challenges and Opportunities. *Prog. Energy Combust. Sci.* **2011**, *37* (2), 113–124.

https://doi.org/10.1016/j.pecs.2010.05.001.
(34) Neyts, E. C. Plasma-Surface Interactions in Plasma Catalysis. *Plasma Chem. Plasma Process.* **2016**, *36* (1), 185–212. https://doi.org/10.1007/s11090-015-9662-5.
(35) Whitehead, J. C. Plasma-Catalysis: Is It Just a Question of Scale? *Front. Chem. Sci. Eng.* **2019**, *13* (2), 264–273. https://doi.org/10.1007/s11705-019-1794-3.
(36) Giammaria, G.; Van Rooij, G.; Lefferts, L. Plasma Catalysis: Distinguishing between Thermal and Chemical Effects. *Catalysts* **2019**, *9*, 185. https://doi.org/10.3390/catal9020185.
(37) Uytdenhouwen, Y.; Meynen, V.; Cool, P.; Bogaerts, A. The Potential Use of Core-Shell Structured Spheres in a Packed-Bed DBD Plasma Reactor for $CO_2$ Conversion. *Catalysts* **2020**, *10* (5), 1–15. https://doi.org/10.3390/catal10050530.
(38) Vakili, R.; Gholami, R.; Stere, C. E.; Chansai, S.; Chen, H.; Holmes, S. M.; Jiao, Y.; Hardacre, C.; Fan, X. Environmental Plasma-Assisted Catalytic Dry Reforming of Methane (DRM) over Metal-Organic Frameworks (MOFs)-Based Catalysts. *Appl. Catal. B Environ.* **2020**, *260*, 118195.
(39) Michielsen, I.; Uytdenhouwen, Y.; Bogaerts, A.; Meynen, V. Altering Conversion and Product Selectivity of Dry Reforming of Methane in a Dielectric Barrier Discharge by Changing the Dielectric Packing Material. *Catalysts* **2019**, *9* (1), 51. https://doi.org/10.3390/catal9010051.
(40) Vakili, R.; Gibson, E. K.; Chansai, S.; Xu, S.; Al-Janabi, N.; Wells, P. P.; Hardacre, C.; Walton, A.; Fan, X. Understanding the CO Oxidation on Pt Nanoparticles Supported on MOFs by Operando XPS. *ChemCatChem* **2018**, *10* (19), 4238–4242. https://doi.org/10.1002/cctc.201801067.
(41) Chen, H.; Mu, Y.; Shao, Y.; Chansai, S.; Xu, S.; Stere, C. E.; Xiang, H.; Zhang, R.; Jiao, Y.; Hardacre, C.; Fan, X. Coupling Non-Thermal Plasma with Ni Catalysts Supported on BETA Zeolite for Catalytic $CO_2$ Methanation. *Catal. Sci. Technol.* **2019**, *9* (15), 4135–4145. https://doi.org/10.1039/c9cy00590k.
(42) Ahmad, F.; Lovell, E. C.; Masood, H.; Cullen, P. J.; Ostrikov, K. K.; Scott, J. A.; Amal, R. Low-Temperature $CO_2$ Methanation: Synergistic Effects in Plasma-Ni Hybrid Catalytic System. *ACS Sustain. Chem. Eng.* **2020**, *8* (4), 1888–1898. https://doi.org/10.1021/acssuschemeng.9b06180.
(43) Álvarez, A.; Borges, M.; Corral-Pérez, J. J.; Olcina, J. G.; Hu, L.; Cornu, D.; Huang, R.; Stoian, D.; Urakawa, A. $CO_2$ Activation over Catalytic Surfaces. *ChemPhysChem* **2017**, *18* (22), 3135–3141. https://doi.org/10.1002/cphc.201700782.
(44) Matthaiou, V.; Oulego, P.; Frontistis, Z.; Collado, S.; Hela, D.; Konstantinou, I. K.; Diaz, M.; Mantzavinos, D. Valorization of Steel Slag towards a Fenton-like Catalyst for the Degradation of Paraben by Activated Persulfate. *Chem. Eng. J.* **2019**, *360*, 728–739. https://doi.org/10.1016/j.cej.2018.11.198.
(45) Ding, R.; Qi, L.; Jia, M.; Wang, H. Facile Synthesis of Mesoporous Spinel $NiCo_2O_4$ Nanostructures as Highly Efficient Electrocatalysts for Urea Electro-Oxidation. *Nanoscale* **2014**, *6* (3), 1369–1376. https://doi.org/10.1039/c3nr05359h.
(46) Kadari, A.; Mahi, K.; Mostefa, R.; Badaoui, M.; Mameche, A.; Kadri, D. Optical and Structural Properties of Mn Doped MgO Powders Synthesized by Sol-Gel Process. *J. Alloys Compd.* **2016**, *688*, 32–36. https://doi.org/10.1016/j.jallcom.2016.07.040.
(47) Prabaharan, D. D. M.; Sadaiyandi, K.; Mahendran, M.; Sagadevan, S. Precipitation Method and Characterization of Cobalt Oxide Nanoparticles. *Appl. Phys. A* **2017**, *123* (264).

https://doi.org/10.1007/s00339-017-0786-8.
(48) Deori, K.; Deka, S. Morphology Oriented Surfactant Dependent CoO and Reaction Time Dependent $Co_3O_4$ Nanocrystals from Single Synthesis Method and Their Optical and Magnetic Properties. *CrystEngComm* **2013**, *15*, 8465–8474. https://doi.org/10.1039/c3ce41502c.
(49) Jayakumar, M.; Hemalatha, K.; Chander, A. A.; Sahu, A. K.; Prakash, A. S. Origin of Charge Storage in Cobalt Oxide - Anchored Graphene Nanocomposites. *Carbon N. Y.* **2017**, *125*, 168–179. https://doi.org/10.1016/j.carbon.2017.09.002.
(50) Dercz, G.; Prusik, K.; Pajak, L.; Pielaszek, R.; Malinowski, J. J.; Pudlo, W. Structure Studies on Nanocrystalline Powder of MgO Xerogel Prepared by the Sol-Gel Method. *Mater. Sci. Pol.* **2009**, *27* (1), 201–207.
(51) Huang, J.; Qian, W.; Ma, H.; Zhang, H.; Ying, W. Highly Selective Production of Heavy Hydrocarbons over Cobalt-Graphene-Silica Nanocomposite Catalysts. *RSC Adv.* **2017**, *7* (53), 33441–33449. https://doi.org/10.1039/c7ra05887j.
(52) Biesinger, M. C.; Payne, B. P.; Grosvenor, A. P.; Lau, L. W. M.; Gerson, A. R.; Smart, R. S. C. Resolving Surface Chemical States in XPS Analysis of First Row Transition Metals, Oxides and Hydroxides: Cr, Mn, Fe, Co and Ni. *Appl. Surf. Sci.* **2011**, *257* (7), 2717–2730. https://doi.org/10.1016/j.apsusc.2010.10.051.
(53) Wang, H. Y.; Ruckenstein, E. CO2 Reforming of CH4 over Co/MgO Solid Solution Catalysts — Effect of Calcination Temperature and Co Loading. *Appl. Catal.* **2001**, *209*, 207–215. https://doi.org/https://doi.org/10.1016/S0926-860X(00)00753-5.
(54) Hosseini, S.; Niaei, A.; Salari, D. Preparation and Characterization of Nano- and Non-Nanoscale Co3O4 Spinels Obtained from Different Methods and Study of Their Performance in Combustion of Aromatics from Polluted Air-A Comparison with Pt/γ-$Al_2O_3$. *J. Environ. Sci. Heal. Part A* **2012**, *47* (12), 1728–1732. https://doi.org/10.1080/10934529.2012.689184.
(55) Ruckenstein, E.; Wang, H. . Carbon Dioxide Reforming of Methane to Synthesis Gas over Supported Cobalt Catalysts. *Appl. Catal. A Gen.* **2000**, *204* (2), 257–263. https://doi.org/10.1016/S0926-860X(00)00674-8.
(56) Thommes, M.; Kaneko, K.; Neimark, A. V.; Olivier, J. P.; Rodriguez-Reinoso, F.; Rouquerol, J.; Sing, K. S. W. Physisorption of Gases, with Special Reference to the Evaluation of Surface Area and Pore Size Distribution (IUPAC Technical Report). *Pure Appl. Chem.* **2015**, *87* (9–10), 1051–1069. https://doi.org/10.1515/pac-2014-1117.
(57) Zeng, Y.; Tu, X. Plasma-Catalytic $CO_2$ Hydrogenation at Low Temperatures. *IEEE Trans. Plasma Sci.* **2016**, *44* (4), 405–411. https://doi.org/10.1109/TPS.2015.2504549.
(58) De Bie, C.; Van Dijk, J.; Bogaerts, A. $CO_2$ Hydrogenation in a Dielectric Barrier Discharge Plasma Revealed. *J. Phys. Chem. C* **2016**, *120* (44), 25210–25224. https://doi.org/10.1021/acs.jpcc.6b07639.
(59) Aerts, R.; Somers, W.; Bogaerts, A. Carbon Dioxide Splitting in a Dielectric Barrier Discharge Plasma: A Combined Experimental and Computational Study. *ChemSusChem* **2015**, *8* (4), 702–716. https://doi.org/10.1002/cssc.201402818.
(60) Xu, S.; Chansai, S.; Shao, Y.; Xu, S.; Wang, Y. chi; Haigh, S.; Mu, Y.; Jiao, Y.; Stere, C. E.; Chen, H.; Fan, X.; Hardacre, C. Mechanistic Study of Non-Thermal Plasma Assisted $CO_2$ Hydrogenation over Ru Supported on MgAl Layered Double Hydroxide. *Appl. Catal. B Environ.* **2020**, *268*, 118752. https://doi.org/10.1016/j.apcatb.2020.118752.
(61) Azzolina-Jury, F.; Thibault-Starzyk, F. Mechanism of Low Pressure Plasma-Assisted $CO_2$

Hydrogenation Over Ni-USY by Microsecond Time-Resolved FTIR Spectroscopy. *Top. Catal.* **2017**, *60* (19–20), 1709–1721. https://doi.org/10.1007/s11244-017-0849-2.

(62) Behrens, M.; Studt, F.; Kasatkin, I.; Kühl, S.; Hävecker, M.; Abild-pedersen, F.; Zander, S.; Girgsdies, F.; Kurr, P.; Kniep, B.; Tovar, M.; Fischer, R. W.; Nørskov, J. K.; Schlögl, R. The Active Site of Methanol Synthesis over Cu/ZnO/$Al_2O_3$ Industrial Catalysts. *Science (80-. ).* **2012**, *336*, 893–897.

(63) Parastaev, A.; Hoeben, W. F. L. M.; van Heesch, B. E. J. M.; Kosinov, N.; Hensen, E. J. M. Temperature-Programmed Plasma Surface Reaction: An Approach to Determine Plasma-Catalytic Performance. *Appl. Catal. B Environ.* **2018**, *239* (July), 168–177. https://doi.org/10.1016/j.apcatb.2018.08.011.

(64) Kattel, S.; Yan, B.; Chen, J. G.; Liu, P. CO2 Hydrogenation on Pt, Pt/$SiO_2$ and Pt/TiO2: Importance of Synergy between Pt and Oxide Support. *J. Catal.* **2016**, *343*, 115–126. https://doi.org/10.1016/j.jcat.2015.12.019.

(65) Zhang, M.; Wu, Y.; Dou, M.; Yu, Y. A DFT Study of Methanol Synthesis from $CO_2$ Hydrogenation on the Pd(111) Surface. *Catal. Letters* **2018**, *148* (9), 2935–2944. https://doi.org/10.1007/s10562-018-2497-y.

(66) Liu, X.; Wang, M.; Zhou, C.; Zhou, W.; Cheng, K.; Kang, J.; Zhang, Q.; Deng, W.; Wang, Y. Selective Transformation of Carbon Dioxide into Lower Olefins with a Bifunctional Catalyst Composed of $ZnGa_2O_4$ and SAPO-34. *Chem. Commun.* **2017**, *54* (2), 140–143. https://doi.org/10.1039/c7cc08642c.

(67) Larmier, K.; Liao, W.-C.; Tada, S.; Lam, E.; Verel, R.; Bansode, A.; Urakawa, A.; Comas-Vives, A.; Copéret, C. $CO_2$-to-Methanol Hydrogenation on Zirconia-Supported Copper Nanoparticles: Reaction Intermediates and the Role of the Metal-Support Interface. *Angew. Chem.* **2017**, *129* (9), 2358–2363. https://doi.org/10.1002/ange.201610166.

(68) Díez, V. K.; Apesteguía, C. R.; Di Cosimo, J. I. Effect of the Chemical Composition on the Catalytic Performance of $Mg_yAlO_x$ Catalysts for Alcohol Elimination Reactions. *J. Catal.* **2003**, *215* (2), 220–233. https://doi.org/10.1016/S0021-9517(03)00010-1.

(69) Gadge, S. T.; Mishra, A.; Gajengi, A. L.; Shahi, N. V.; Bhanage, B. M. Magnesium Oxide as a Heterogeneous and Recyclable Base for the N-Methylation of Indole and O-Methylation of Phenol Using Dimethyl Carbonate as a Green Methylating Agent. *RSC Adv.* **2014**, *4* (91), 50271–50276. https://doi.org/10.1039/c4ra07240e.

(70) Wang, L.; Wang, L.; Zhang, J.; Liu, X.; Wang, H.; Zhang, W.; Yang, Q.; Ma, J.; Dong, X.; Yoo, S. J.; Kim, J. G.; Meng, X.; Xiao, F. S. Selective Hydrogenation of $CO_2$ to Ethanol over Cobalt Catalysts. *Angew. Chem. Int. Ed.* **2018**, *57* (21), 6104–6108. https://doi.org/10.1002/anie.201800729.

(71) Wang, L.; He, S.; Wang, L.; Lei, Y.; Meng, X.; Xiao, F.-S. Cobalt-Nickel Catalysts for Selective Hydrogenation of Carbon Dioxide into Ethanol. *ACS Catal.* **2019**, *9*, 11335–11340. https://doi.org/10.1021/acscatal.9b04187.

(72) Melaet, G.; Ralston, W. T.; Li, C. S.; Alayoglu, S.; An, K.; Musselwhite, N.; Kalkan, B.; Somorjai, G. A. Evidence of Highly Active Cobalt Oxide Catalyst for the Fischer-Tropsch Synthesis and $CO_2$ Hydrogenation. *J. Am. Chem. Soc.* **2014**, *136* (6), 2260–2263. https://doi.org/10.1021/ja412447q.

(73) Jimenez, J.; Bird, A.; Santos Santiago, M.; Wen, C.; Lauterbach, J. Supported Cobalt Nanorod Catalysts for Carbon Dioxide Hydrogenation. *Energy Technol.* **2017**, *5*, 884–891. https://doi.org/10.1002/ente.201600575.

(74) Ma, X.; Li, S.; Ronda-Lloret, M.; Chaudhary, R.; Lin, L.; van Rooij, G.; Gallucci, F.;

Rothenberg, G.; Shiju, N. R.; Hessel, V. Plasma Assisted Catalytic Conversion of $CO_2$ and $H_2O$ Over $Ni/Al_2O_3$ in a DBD Reactor. *Plasma Chem. Plasma Process.* **2019**, *39*, 109–124. https://doi.org/10.1007/s11090-018-9931-1.

(75) Liu, S.; Winter, L. R.; Chen, J. G. Review of Plasma-Assisted Catalysis for Selective Generation of Oxygenates from $CO_2$ and $CH_4$. *ACS Catal.* **2020**, *10* (4), 2855–2871. https://doi.org/10.1021/acscatal.9b04811.

(76) Wang, Y.; Craven, M.; Yu, X.; Ding, J.; Bryant, P.; Huang, J.; Tu, X. Plasma-Enhanced Catalytic Synthesis of Ammonia over a $Ni/Al_2O_3$ Catalyst at Near-Room Temperature: Insights into the Importance of the Catalyst Surface on the Reaction Mechanism. *ACS Catal.* **2019**, 10780–10793. https://doi.org/10.1021/acscatal.9b02538.
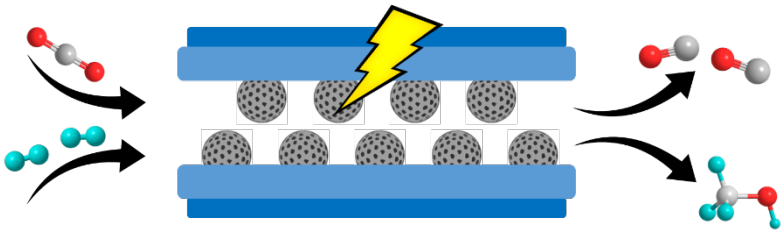
Table of Contents Use Only $CO_2$ hydrogenation to CO and methanol was achieved near room temperature and atmospheric pressure using plasma-enhanced catalysis. The catalyst metal loading and cobalt oxide dispersion influence the product distribution.